Bioelectrical model of head-tail patterning based on cell ion channels and intercellular gap junctions

Javier Cervera[1,*], Salvador Meseguer[2], Michel Levin[3], Salvador Mafe[1]

[1]Dept. de Termodinàmica, Facultat de Física, Universitat de València, E-46100 Burjassot, Spain.

[2]Laboratory of Immunobiology, Centro de Investigación Príncipe Felipe, Valencia 46012, Spain.

[3]Allen Discovery Center at Tufts University, Department of Biology, Tufts University Medford, Massachusetts 02155-4243, United States. (ORCID: 0000-0001-7292-8084)

[*]Corresponding author:

E-mail address: jcervera@uv.es (Javier Cervera)

Abstract

Robust control of anterior-posterior axial patterning during regeneration is mediated by bioelectric signaling. However, a number of systems-level properties of bioelectrochemical circuits, including stochastic outcomes such as seen in permanently de-stabilized “cryptic” flatworms, are not completely understood. We present a bioelectrical model for head-tail patterning that combines *single-cell* characteristics such as membrane ion channels with *multicellular community* effects via voltage-gated gap junctions. It complements the biochemically-focused models by describing the effects of intercellular electrochemical coupling, cutting plane, and gap junction blocking of the multicellular ensemble. We provide qualitative insights into recent experiments concerning planarian anterior/posterior polarity by showing that: (*i*) bioelectrical signals can help separated cell domains to know their relative position after injury and contribute to the transitions between the abnormal double-head state and the normal head–tail state; (*ii*) the bioelectrical phase-space of the system shows a bi-stability region that can be interpreted as the cryptic system state; and (*iii*) context-dependent responses are obtained depending on the cutting plane position, the initial bioelectrical state of the multicellular system, and the intercellular connectivity. The model reveals how simple bioelectric circuits can exhibit complex tissue-level patterning and suggests strategies for regenerative control in vivo and in synthetic biology contexts.

Keywords:

bioelectricity, ion channel, head-tail patterning, positional information, regeneration, gap junctional communication

Highlights:

- A bioelectrical model of head-tail axial patterning in regeneration is presented
- The model combines single-cell characteristics with multicellular community effects
- Qualitative insights are given concerning planarian anterior/posterior polarity
- Bioelectrical signals help cell domains to know their relative position after injury
- The model exhibits complex tissue-level patterns suggesting regenerative strategies

Graphical abstract:

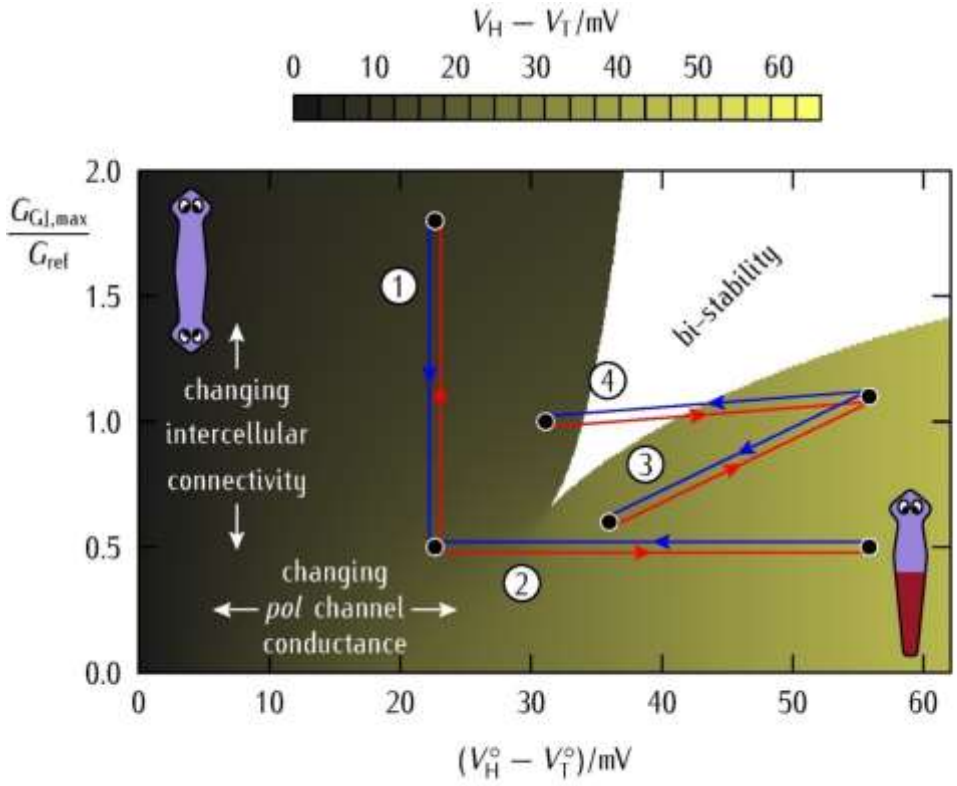

Bioelectrical phase space of head-tail axial patterning for planaria.

1. Introduction

Axial patterning processes, such as those that establish the head and tail ends of regenerating fragments of animals or plants, are commonplace in biology and have traditionally been described using biochemical approaches based on the spatio-temporal distribution of specific morphogens; see e.g. [1-3] and references therein for the particular case of head-tail development in planaria. A perennial question concerns the mechanisms that align and establish robust biochemical gradients, and the means by which bioelectrical signaling can influence shape and contribute to re-specify the distribution of signaling ions and molecules [4-8]. The mechanisms behind the emergence of a pattern are not easy to identify and control because real biological networks include many feedbacks [4,5,9-11]. In this context, simple biophysical circuits can be useful because they typically involve a small number of basic equations and average magnitudes such as electric potentials and ionic concentrations [12,13], and reveal the minimal components that are sufficient to implement specific system-level behaviors. In addition, the external regulation of these magnitudes defined at the multicellular level may allow the modulation of the system state without the need of acting at the single-cell molecular level [13-15], facilitating the control of large-scale outcomes in vivo or in synthetic bioengineering settings.

Here, we make use of an approach that emphasizes bioelectrical *single-cell* characteristics such as membrane ion channels and pumps, including also *multicellular community* effects via voltage-gated gap junctions [13]. In this way, the effects of different counteracting channels, variable intercellular connectivity, and tissue cutting plane [4,14,16] are explicitly dealt with. Despite the above features, the model is purely bioelectrical (lacks biochemical signals and processes operating in real biological systems [1,2,17,18]) and thus is not a bio-realistic simulation; rather, it reveals the minimal bioelectric circuit needed to provide complex dynamics that show biologically-relevant features. A future goal would be to relate the vector transport fields of detailed transport models [17] with the simple electrical approaches used here because in real systems biochemical and bioelectrical signals act in concert.

For the particular case of the planaria system, different computational procedures focused on flatworm regeneration have been presented. In particular, previous theoretical models have considered the role of nerve fibers [17], studied the stable attractors defined in a body morphospace [15,16], and identified the different outcomes using reverse-engineering methods and bioinformatics concepts focused on gene-regulatory networks [19]. Although a complete description of specific anatomical outcomes requires accounting for the redistribution of the biochemical signals that establish head-to-tail (H–T) polarities [1-3], the fact is that bioelectric signals and gradients play a key role in signal transmission, development, and regeneration, as observed in plants [20], the development of systems from insects to humans and, in particular, in planaria regeneration [4,7,14,16]. This role has been emphasized in the case of anterior/posterior polarity [4,14,17]; below, we qualitatively discuss some of the results obtained in the light of recent planaria experiments shown in Schematic 1 (see Fig. 5 of Ref. [14] for details).

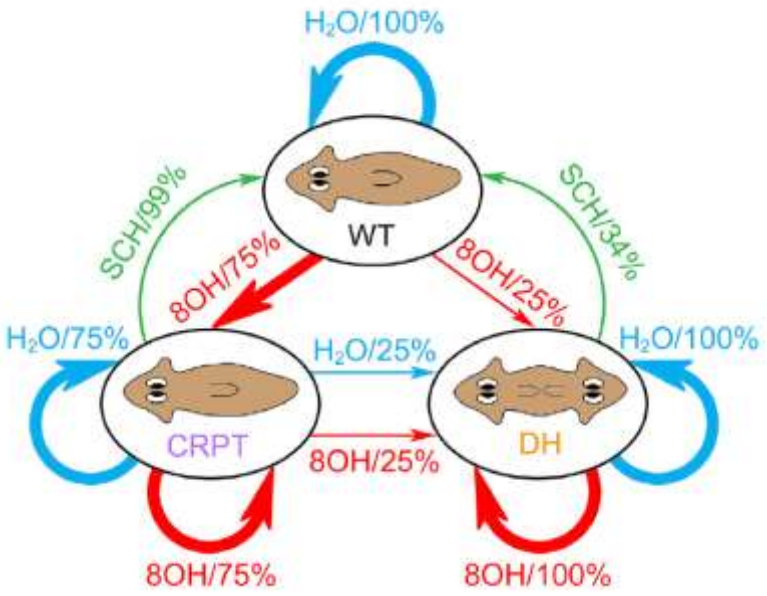

Schematic 1. The change in target morphology we will refer to in the text [14]. Note the remarkable fact that after being once treated with an inhibitor of electrical synapses (the gap junction blocker 8OH), worms regenerate in one of two states: a two-headed form, or a one-headed form which has apparently normal anatomy but a de-stabilized, stochastic ("cryptic") target morphology encoding: in

subsequent cuts, these will again stochastically form 2-headed or cryptic worms. The percentages of phenotype CRPT (cryptic/WT) or DH (double head) were obtained from pharyngeal fragments treated in a blocker (octanol, 8-OH) of the gap junctions, a H,K-ATPase inhibitor (SCH-28080), or water. The wild-type (WT) would correspond to the normal head-tail (H–T) phenotype here. While the DH phenotype is permanent (regenerating as 2-headed in subsequent cuts in plain water), the cryptic planarian regeneration is stochastic with characteristic (and persistent, through multiple rounds of regeneration) transition probabilities. Reproduced from Durant *et al.* (2017). Long-Term, Stochastic Editing of Regenerative Anatomy via Targeting Endogenous Bioelectric Gradients. Biophys J. 112, 2231–2243. Biophysical Society.

While existing models explain the results of numerous perturbations leading to alterations of the normal head-tail axis (see, in particular, the thorough study of Ref. [17] and references therein), one fundamental observation has not been explored with detail as the emerging property of a bioelectric circuit: the role of cryptic states and stochastic outcomes in the system phase space (Schematic 1). In planaria treated briefly with gap junctional inhibitors, an entire region of cells (one end of a cut fragment) forms a head or tail with a given probability despite macroscopically identical starting conditions – the process is “random” but at the level of the entire fragment: all cells agree on which outcome has been chosen. We will explore the cryptic state characteristics in the context of the bioelectric phase space establishing the head-tail configuration. Rather than describing growing processes and the ionic currents involved, we discuss how bioelectric fields could assist them by establishing patterns.

Experimentally, the spatio-temporal distribution of those signaling ions and molecules that regulate crucial downstream biochemical pathways can be influenced by multicellular electric potential maps qualitatively similar to those obtained here. Therefore, these maps would act as *distributed controllers* encoding specific spatial patterns that are eventually decoded as different biological outcomes [13,15,21,22]. In this case, however, the experimental times must be longer than those in the simulations where the spreading of purely bioelectrical signals over small multicellular regions takes

about 10 s only. In real systems, times longer than those obtained here should be observed because of the following additional effects:

1. *slow* diffusion + reaction processes may be coupled with relatively *fast* electrical processes;
2. biological systems may have "stabilizing checkpoints" not accounted for in the model that oppose the spread of the electrical perturbations; and
3. the number of cells in typical experimental systems is much larger than that considered here. For instance, a monolayer of 10^4 – 10^5 cells can give responses on the order of hours or days if genetic downstream pathways and subsequent growing phenomena are incorporated in the model.

To better identify the main bioelectrical characteristics regulating the different system outcomes, we study first a two-cell model before considering the whole multicellular ensemble. This simple system allows an immediate biophysical understanding that proves to be useful for the more complex phenomena that arises in coupled multicellular ensembles [13,17].

2. Two-cell model results

Consider the two-cell model of Schematic 2, which is based on previous studies describing the effects of the gap junction nonlinearities in coupled cells [13,21-23]. Regions H and T consist of only a single cell whose state is described by the respective cell electric potentials V_H and V_T, defined as the negative potential difference between the cell inside and the external microenvironment. These single-cell potentials result from the current balance established between two generic *dep* and *pol* ion channels, an ion pump, and the intercellular gap junction (Schematic 2). The *dep* and *pol* channel conductances, assumed to be constant only for the case of the two-cell model, act to establish the ionic equilibrium potentials E_{dep} and E_{pol} that characterize the *depolarized* and *polarized* cell potentials, respectively. The pump is assumed to maintain the ionic concentration differences between the cell

inside and the extracellular media that support the above equilibrium potentials. The intercellular current through the gap junction aims at eliminating the potential difference between the two neighboring cells. However, the voltage-gated junction conductance of Schematic 2 is not constant but takes low values when the difference $V_H - V_T$ between the H and T cell potentials is sufficiently high, allowing this difference to be maintained because of the junction closure (Schematic 3, *left*). It is this experimental fact that permits the electric potential regionalization in the model [13,22].

Membrane surface exposed proteins can act through conformational changes, specific ligand-gated effects, and other non-conductive mechanisms. In particular, ion channels can also have other functions in addition to their ion conductive properties, e.g. those based on the interaction with various biomolecules. Although Schematic 2, focuses on the channel conductive mechanisms, we note that the regulation of ion channel conductance by the interaction with other molecules can also be accounted for by changing the effective values of the *dep* and *pol* channel conductances in the simulation [13,22]. A leakage can also be incorporated by including an additional constant channel conductance in the model of Schematic 2 [13], as shown in the *Supplementary Information*. In addition, the particular expressions of the different ion channel proteins could also be incorporated explicitly in the bioelectrical model at the price of increasing complexity [21]. In this case, a range of response times from rapid electrical relaxations on the order of seconds to slow genetic processes on the order of hours are obtained [21,22]. In our case, we will concentrate only on the *bioelectrical maps*, assuming that these *initial pre-patterns* will eventually result state into downstream biochemical, transcriptional, and epigenetic changes in the long term [4,13,21,22]. It is in this way that temporary bioelectric interventions should have long-lasting effects.

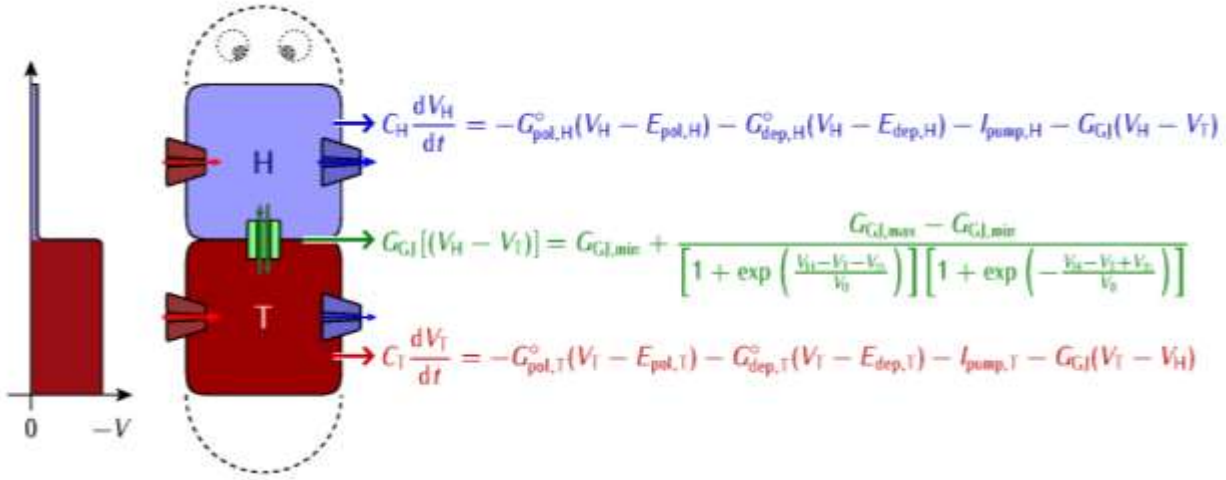

Schematic 2. A two-cell model for the head (H)–tail (T) bioelectrical regionalization. The H-cell capacitance is denoted by C_{H} . The H-cell potential V_{H} may change with time *t* because of the current balance between two generic *pol* and *dep* channels of constant conductances $G^{\circ}_{\mathrm{pol,H}}$ and $G^{\circ}_{\mathrm{dep,H}}$, a pump of current $I_{\mathrm{pump,H}}$, and the intercellular current across the H–T gap junction of voltage-gated conductance G_{GJ}. Note that we use the brackets in the function $G_{\mathrm{GJ}}[(V_{\mathrm{H}} - V_{\mathrm{T}})]$ to indicate that this conductance is voltage-gated by the intercellular potential difference $(V_{\mathrm{H}} - V_{\mathrm{T}})$. Similar equations can be written for the T-cell potential V_{T}. The left schematic shows the electric potential difference between the head and tail cells.

Schematic 3 shows the *phase space* obtained from the solution of the equations system of Schematic 2. We denote by $V^{\circ}_{\mathrm{H}} - V^{\circ}_{\mathrm{T}}$ the two-cell potential difference obtained when cells H and T are *isolated* from each other and then $G_{\mathrm{GJ}} = 0$ in Schematic 2. This *reference* potential difference, together with the *maximum* gap junction conductance $G_{\mathrm{GJ,max}}$, are the system variables that determine the bioelectrical states in the phase space of Schematic 3.

Many bioelectrical characteristics may influence the H–T potential difference (Schematic 2). In our case, we obtain the different values of $V^{\circ}_{\mathrm{H}} - V^{\circ}_{\mathrm{T}}$ of Schematic 3 by changing only the *pol* channel conductance of the H cell ($G^{\circ}_{\mathrm{pol,H}}$) of Schematic 2. Therefore, the *pol* channel conductance of the T cell $G^{\circ}_{\mathrm{pol,T}}/G_{\mathrm{ref}} = 4.0$, the equilibrium potentials $E_{\mathrm{dep,H}} = E_{\mathrm{dep,T}} = 0$ and $E_{\mathrm{pol,H}} = E_{\mathrm{pol,T}} = -70$ mV, and the *dep* channel conductances $G_{\mathrm{dep,H}}/G_{\mathrm{ref}} = G_{\mathrm{dep,T}}/G_{\mathrm{ref}} = 0.5$ are kept constant. In a similar way, the

effect of the intercellular gap junction is simulated by modifying the maximum conductance $G_{\mathrm{GJ,max}}/G_{\mathrm{ref}}$ between 0.2 and 2.0 (Schematic 3, left), keeping constant the rest of junction parameters: $G_{\mathrm{GJ,min}}/G_{\mathrm{ref}} = 0.2$ for the minimum conductance, $V_{\mathrm{th}} = 20$ mV for the threshold potential, and $V_0 = 2$ mV for the width potential (Schematic 2). Note that we have expressed all conductances in terms of the reference value G_{ref} to better discuss their relative roles. For reference conductances in the range $G_{\mathrm{ref}} = 0.1 - 1$ nS and cell capacitances $C_{\mathrm{H}} = C_{\mathrm{T}} = 100$ pF, the electric time responses are on the order of $C_{\mathrm{H}}/G_{\mathrm{ref}} = 0.1 - 1$ s for a single-cell.

As expected, Schematic 3 shows that the H–T potential difference $V_{\mathrm{H}} - V_{\mathrm{T}}$ (points of the phase space) increases with the isolated cells potential difference $V_{\mathrm{H}}^{\circ} - V_{\mathrm{T}}^{\circ}$ (*horizontal* axis). As to the maximum gap junction conductance $G_{\mathrm{GJ,max}}/G_{\mathrm{ref}}$ (*vertical* axis), it attempts to establish the isopotential condition $V_{\mathrm{H}} = V_{\mathrm{T}}$ because of the intercellular currents in Schematic 2. Note however that the effective conductance $G_{\mathrm{GJ}}[(V_{\mathrm{H}} - V_{\mathrm{T}})]$ is voltage-gated and this experimental fact can lead to the closure of the gap junction for sufficiently high $V_{\mathrm{H}} - V_{\mathrm{T}}$ values (Schematic 3, *left*). The phase space of Schematic 3 is in qualitative agreement with a previous study on the effects of the gap junction nonlinearities in coupled cells [23].

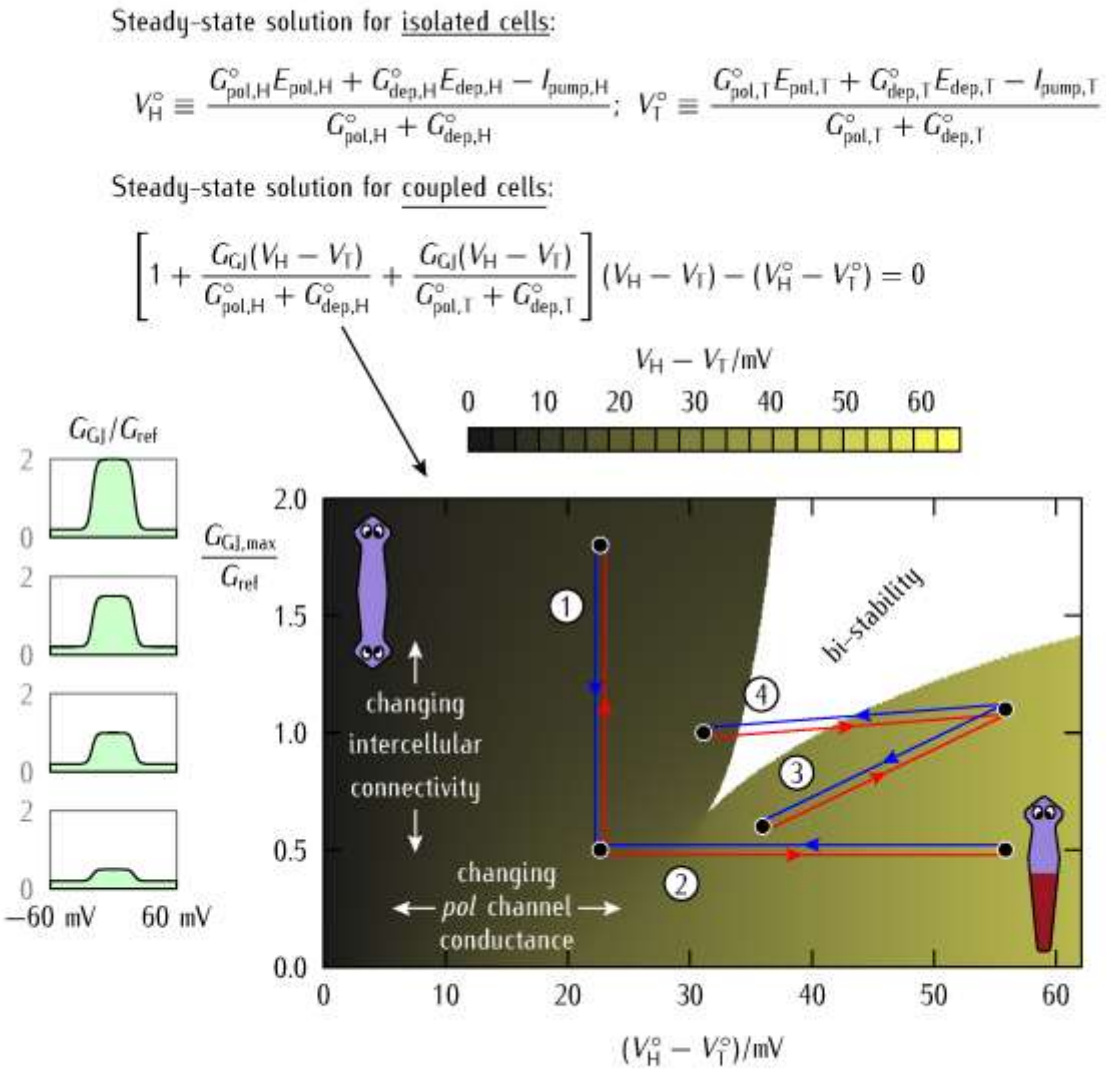

Schematic 3. Equations for the steady state potentials of the isolated (V_H°, V_T°) and coupled (V_H, V_T) H and T cells (*top*). As a first approximation, we neglect the contribution of the pump currents to the potentials (V_H°, V_T°) and assume that the only role of the pumps is to keep constant the ionic concentrations that produce the equilibrium potentials $(E_{pol,H}, E_{pol,T})$. Note also that the values of the potentials (V_H°, V_T°) should be introduced in the implicit equation to be solved for the potential difference $V_H - V_T$ .This procedure gives the phase space for the potential difference $V_H - V_T$ as a function of the isolated cells potential difference $V_H^\circ - V_T^\circ$ and the maximum gap junction conductance $G_{GJ,max}/G_{ref}$ (*bottom*). The left schematic shows the voltage-gated gap junction conductances calculated from the equation for G_{GJ} of Schematic 2 for the maximum conductances $G_{GJ,max}/G_{ref}$ shown in the ordinate

axis. The color gradient indicates the different monostable solutions for $V_{\mathrm{H}} - V_{\mathrm{T}}$ while the central white zone corresponds to the bi-stability region where three solutions, two stable and one unstable, are possible. The arrows show the direct and inverse trajectories of *four* bioelectric processes: (1) at constant $V_{\mathrm{H}}^{\circ} - V_{\mathrm{T}}^{\circ}$, (2) at constant $G_{\mathrm{GJ,max}}/G_{\mathrm{ref}}$, (3) out of the bi-stability region, and (4) across the bi-stability region. The insets explain the relevant experimental magnitudes that change along these trajectories.

Schematic 3 suggests that weakening the intercellular conductance by external blocking of the gap junctions can be modeled by decreasing the maximum junction conductance $G_{\mathrm{GJ,max}}/G_{\mathrm{ref}}$ in the vertical axis (process 1) while adding polarizing/depolarizing ion channels and pumps to the cell membrane can be simulated by changing the potential difference $V_{\mathrm{H}}^{\circ} - V_{\mathrm{T}}^{\circ}$ in the horizontal axis (process 2) [4,14,16,23]. The change in $V_{\mathrm{H}}^{\circ} - V_{\mathrm{T}}^{\circ}$ is achieved through modification of ($G_{\mathrm{pol,H}}^{\circ}$); see Schematic 3 (*top*). Processes 3 and 4 involve the change of both bioelectrical magnitudes out of (process 3) and across (process 4) the bi-stability region. Note that these processes do not indicate any particular regeneration mechanism but only the change in the system bioelectrical state that is supposed to trigger the biochemical pathways leading to the final anatomical outcome.

Remarkably, the model predicts a *central* bi-stability region where *three* mathematical solutions for $V_{\mathrm{H}} - V_{\mathrm{T}}$ are possible, two stable (*high* system polarization and *low* system polarization) and one *unstable* [23]. In this case, the term *high system polarization* makes reference to a *high* $V_{\mathrm{H}} - V_{\mathrm{T}}$ difference and corresponds to the *normal* H–T outcome as opposed to the term *low system polarization* that makes reference to a *low* $V_{\mathrm{H}} - V_{\mathrm{T}}$ difference and could lead to the *abnormal* double head (DH) outcome; see Refs. [4,14,17] for the above experimental morphologies. As to the central bi-stability region, we could tentatively associate it to *cryptic* states where relatively small modifications in the single-cell channels and intercellular conductances can drive significant polarity changes, as suggested by recent experimental data in planarian systems [4,14].

Thus, there is a clear difference between the cryptic and the DH bioelectrical states because the first one may eventually (but not necessarily) lead to the second one under certain conditions

(Schematic 3). In this sense, the cryptic state would act as a *bistable latent memory* whose eventual outcome -the *monostable* H-T and DH states- can be externally tuned by changing the bioelectrical asymmetry described by the potential difference $V_{\mathrm{H}}^{\circ} - V_{\mathrm{T}}^{\circ}$ and/or the intercellular connectivity described by the gap junction conductance $G_{\mathrm{GJ,max}}/G_{\mathrm{ref}}$. This theoretical result offers a qualitative explanation to the heretofore puzzling experimental data on planarian stochastic regenerative outcomes, such as in Fig. 5 of Ref. [14] (reproduced in Schematic 1 here); it suggests that the cryptic state is indeed different from both wild-type and DH states, and shows how bioelectrical transitions between the states can be induced.

In particular, from the qualitative experimental results of Schematic 1 and the two-cell phase space of Schematic 3, we can conclude that:

i. the use of polarizing agents such as H,K-ATPase inhibitors (SCH) that increase the potential difference $V_{\mathrm{H}}^{\circ} - V_{\mathrm{T}}^{\circ}$ at constant gap junction conductance $G_{\mathrm{GJ,max}}/G_{\mathrm{ref}}$ may allow the transition from the abnormal DH state to the normal H–T state of Schematic 3 (process 2); on the contrary, depolarizing agents such as the nigericin ion pump should favor the inverse process. Also, for high enough values of the conductance $G_{\mathrm{GJ,max}}/G_{\mathrm{ref}}$, the above transitions between the DH and H–T states can occur through the *central* bi-stability region of Schematic 3 where cryptic states are possible (compare process 4 with 3);

ii. externally-induced closing of the gap junction by a blocking agent such as octanol leads to low intercellular conductances $G_{\mathrm{GJ,max}}/G_{\mathrm{ref}}$ whose effects are *context-dependent* (processes 1, 3, and 4). At constant *low* potential differences $V_{\mathrm{H}}^{\circ} - V_{\mathrm{T}}^{\circ}$ (*left* side of the *central* bi-stability region of Schematic 3), the decrease of $G_{\mathrm{GJ,max}}/G_{\mathrm{ref}}$ will not change the DH state (process 1). At constant *high* values of $V_{\mathrm{H}}^{\circ} - V_{\mathrm{T}}^{\circ}$ (*central* bi-stability region

of Schematic 3, however, the decrease of $G_{\mathrm{GJ,max}}/G_{\mathrm{ref}}$ may trigger the system transition from the cryptic to the normal H–T state;

iii. when both the potential difference $V_{\mathrm{H}}^{\circ} - V_{\mathrm{T}}^{\circ}$ and the gap junction conductance $G_{\mathrm{GJ,max}}/G_{\mathrm{ref}}$ are simultaneously decreased, the addition of a blocking junction agent may favor the transition from the normal H–T state to the cryptic and abnormal DH states. This transition should be different across the bi-stability region (process 4) than out of the bi-stability region (process 3); and

iv. the model does not give any fixed value for the frequency of DH worms arising from cutting cryptic worms [14]. It is the relative distance of the cryptic state, described by the *point* corresponding to this system state in the bi-stability region of Schematic 3, to the monostable DH (*left*) and H-T (*right*) states that should establish the probability to eventually reach one of these states after cutting. Therefore, the model predicts that acting on: (1) the ion channels and pumps that establish the potential difference $V_{\mathrm{H}}^{\circ} - V_{\mathrm{T}}^{\circ}$ and (2) the gap junction proteins that modulate the intercellular connectivity $G_{\mathrm{GJ,max}}/G_{\mathrm{ref}}$ can shift the above transition probability by changing the relative distance of the cryptic state to the monostable DH (*left*) and H-T (*right*) states of Schematic 3. Note however that this schematic is based on a two-cell model. For a multicellular system, the particular position of the cutting plane may also influence the probability of the final outcome, as we will show later.

The theoretical predictions *i–iv*) appear to be in qualitative agreement with a series of experimental trends reported for planarian systems that are shown in Schematic 1 [4,14]: see Figs. 2, 4, and 5 of Ref. [10] for the octanol inhibition of the gap junctions, the bioelectric characteristics of cryptic planaria,

and the changes in target morphology caused by different external agents, respectively; as well as Figs. 2 and 3 of Ref. [4] for the effects of adding nigericin and the close correspondence between planarian bioelectrics and regenerative outcomes, respectively.

To better understand the changes in the H–T potential difference along the bi-stability region, we consider now the two inverse trajectories described by the arrows of Schematic 3 for the cases of processes 3 (*left*) and 4 (*right*); see Fig. 1 for the potentials V_{H} and V_{T}. Here, process 4 is the most interesting one because it goes across the bi-stability region (Fig. 1, *right*). The steady-state solutions (*light* colors) of potentials V_{H} and V_{T} are also included in Fig. 1 to check that the processes considered here are sufficiently slow to reach these potentials as well as to indicate which branch of the bistable region follow these cell potentials.

Fig. 1 (*right*) shows that the cell potentials V_{H} and V_{T} take their respective branches on entering the bistable region; the V_{H} and V_{T} changes are smooth except for the abrupt steps observed when exiting the bistable region of Schematic 3. Because of this hysteresis, the model predicts that a small change in the relevant bioelectrical parameter (the conductance $G^{\circ}_{\mathrm{pol,H}}$ in the case considered here) can induce a large change on $V_{\mathrm{H}} - V_{\mathrm{T}}$ in one direction only within the bi-stability region –compare the *left* and *right* curves of Fig. 1. Note also that a large modification in the opposite direction is needed to reverse the above change in this case. In general, the hysteresis should depend not only on the single-cell channel conductances but also on the shape of the voltage-gated intercellular conductance [23].

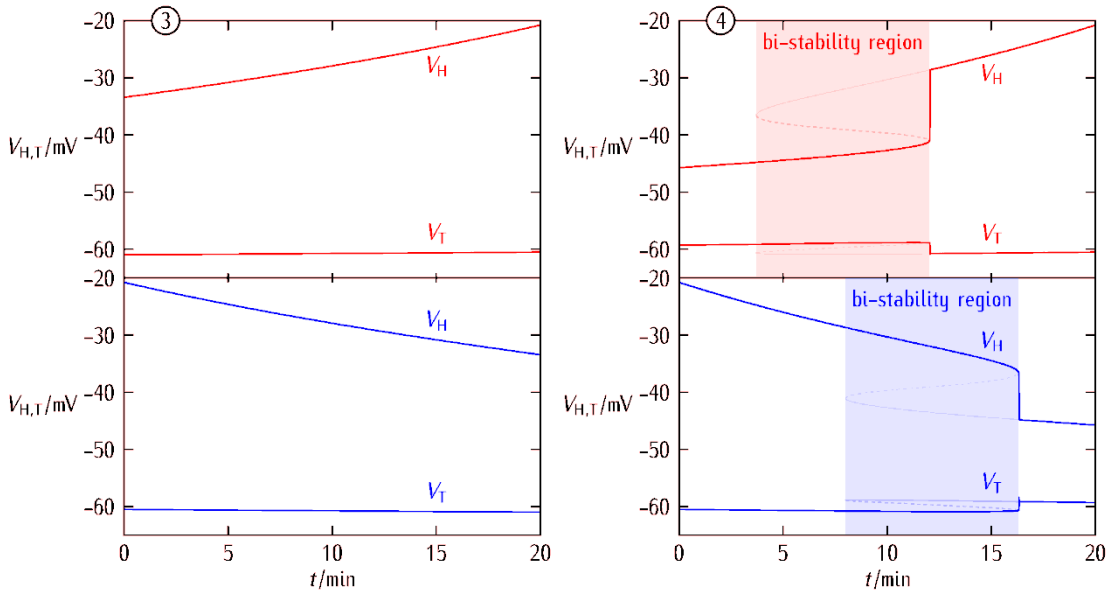

Fig. 1. The time evolution of the H and T cell potentials are shown for the processes 3 (*left*) and 4 (*right*) of Schematic 3. In each process, the two inverse trajectories of Schematic 3 are shown; the *red* and *blue* arrows correspond to the *top* and *bottom* figures here, respectively. In this case, the *pol* channel conductance of the H cell changes slowly with time to achieve the required changes in the H–T potential difference $V_H - V_T$ while the other system parameters are kept constant. The light colors correspond to the steady-state solutions of Schematic 3 and the dark colors give the time trajectory followed by the cell potentials (*right*). The dashed curves correspond to the unstable solutions, which are those related to the hysteresis (*right*). Note that for process 4 (*right*) the *red* curve corresponds to the time evolution from the DH state (low $V_H - V_T$) to the H–T state (high ($V_H - V_T$)), which is just the opposite time evolution described by the *blue* curve. The insets show the different bi-stability regions.

3. Multicellular model results

After the two-cell model of Schematic 2, we consider now a multicellular ensemble of approximately 1000 cells (Schematic 4). The state of a particular cell i in the ensemble is described by its potential V_i whose time variation is modulated by the currents $I_{\mathrm{pol},i}$ and $I_{\mathrm{dep},i}$ of two *pol* and *dep* voltage-gated channels together with the intercellular currents through the gap junctions of the nearest neighbors (nn). The initially (zero time) cell potential is assumed to be that of the isolated cell, which is

calculated from the current balance equation $I_{\mathrm{pol},i} + I_{\mathrm{dep},i} = 0$. This equation is obtained by "switching off" the neighbors ($G_{\mathrm{GJ}} = 0$) and then looking for the steady-state resting potentials. Wherever a cell shows bi-stability so that two stable solutions are possible for the cell potential [21], we choose that solution with the higher absolute value (the *polarized* potential solution).

A complete description of the system equations and parameters, together with the numerical procedures employed to solve them, is given in the *Supplementary Information*. The isolated cell potentials are the initial values introduced in the connected ensemble that is obtained when we "switch on" the influence of the neighbors. The multicellular ensemble is then left to evolve with time by solving about 1000 coupled equations that describe the cell potentials evolution (Schematic 4). The characteristic time of this reduced bioelectric model is of the order of 10 s and thus the ensemble rapidly relaxes to the steady state after 1 min approximately. The nature of this state depends on the single-cell characteristics and the connectivity degree between cells [17,21,22]. See also the *Supplementary Information* for details. In our case, we may observe three different outputs. In principle, the whole ensemble could become either depolarized (low absolute value of the cell potentials) or polarized (high absolute value of these potentials). In many cases, however, the ensemble has a depolarized region at the head and a polarized region at the tail, with a central transition region that is more or less abrupt depending on the closure degree of the intercellular gap junction. Note that this junction may close, thus giving a negligible intercellular conductance, for high absolute values of $V_i - V_j$, where *i* and *j* are two neighboring cells (Schematic 3, *left*).

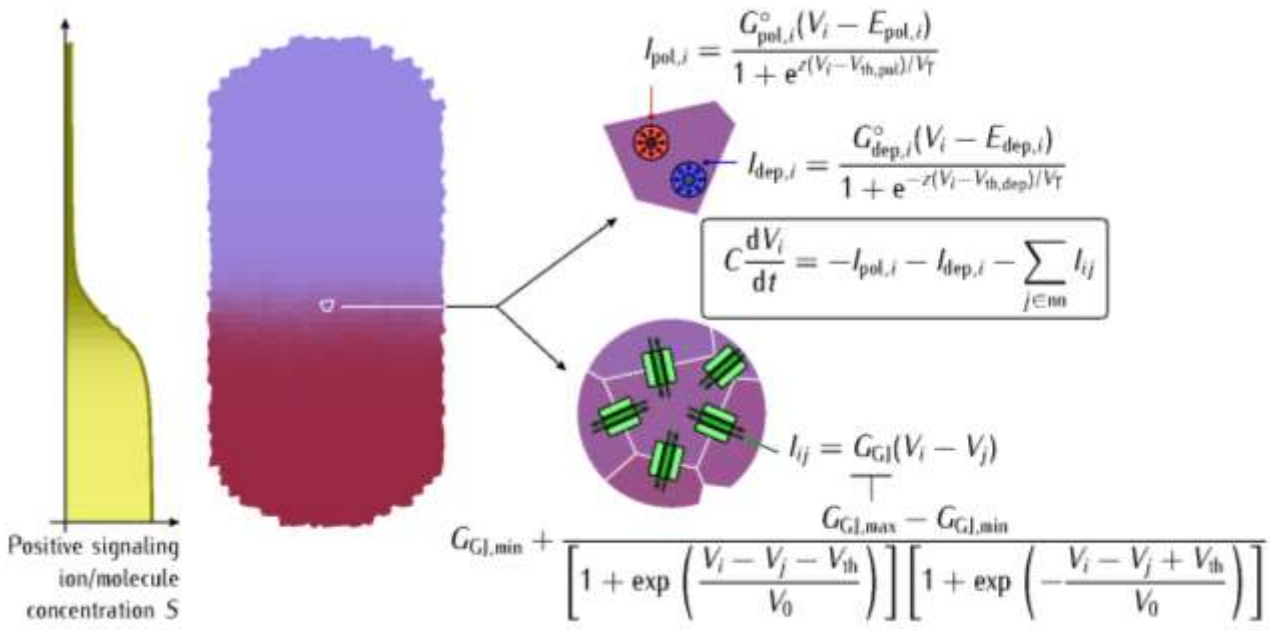

Schematic 4. The multicellular model. Every cell *i* state is described by its potential V_i that changes with time according to the current balance between the *pol* and *dep* voltage-gated channels and the intercellular currents [21]. The number of nearest neighbors (nn) is 5 to 7 cells. The parameters, $V_{\mathrm{th,pol}} = V_{\mathrm{th,dep}} = -27$ mV and $z = 3$ are the channel threshold potentials and the effective number of charges involved in gating, respectively [21,22]. Additional details are given in the *Supplementary Information*. The left schematic shows the concentration profile *S* of a positively charged signaling ion or molecule that is regulated by the electric potential difference between the head and tail cells.

After the system has reached the steady state, we cut three slices of approximately the same size at different positions of the ensemble (Schematic 5). The slices are then left to evolve to the new state, as shown in Schematics 5 and 6. In these two simulations, all the cells have the same properties except for the maximum value of the *pol* channel conductance (G°_{pol}). For the T cells at the bottom, the maximum conductance $G^{\circ}_{\mathrm{pol}}/G_{\mathrm{ref}} \approx 1.4$, while this value decreases linearly as we move upwards to the H cells at the top to reach the lowest value $G^{\circ}_{\mathrm{pol}}/G_{\mathrm{ref}} \approx 0.4$ in Schematic 5 and $G^{\circ}_{\mathrm{pol}}/G_{\mathrm{ref}} \approx 0.3$ in Schematic 6. In both cases, the decrease of G°_{pol} along the vertical axis promotes the depolarized state of the H cells, so that a polarized (tail)-depolarized (head) transition region may appear in the ensemble, as shown by experimental data [4,14]. As expected, Schematic 5 shows a smoother transition

in the central region than that of Schematic 6 because of the voltage dependence of the gap junction conductance (Schematic 3, *left*). This conductance increases, thus favoring the multicellular *community effect* and isopotentiality, when the cells are at similar potentials. On the contrary, the junction conductance decreases, thus favoring the electrically regionalized ensemble, at high intercellular voltage [13,22].

Note also that the ensemble depolarization is the dominant state in Schematics 5 and 6 because the H cells are in a *monostable* depolarized state while the T cells are in a *bistable* region [21,22]. The multicellular community effect can then be clearly seen in the resulting slices: because the depolarized state is the *dominant* one in Schematics 5 and 6, the polarized cells can retain this state only when its number in the slice is high enough (Schematic 6). In this case, both the cell potentials map and the three slices show abrupt transition regions because of the closure of the gap junctions, which occurs only for high enough potential differences between neighboring cells (Schematic 3, *left*).

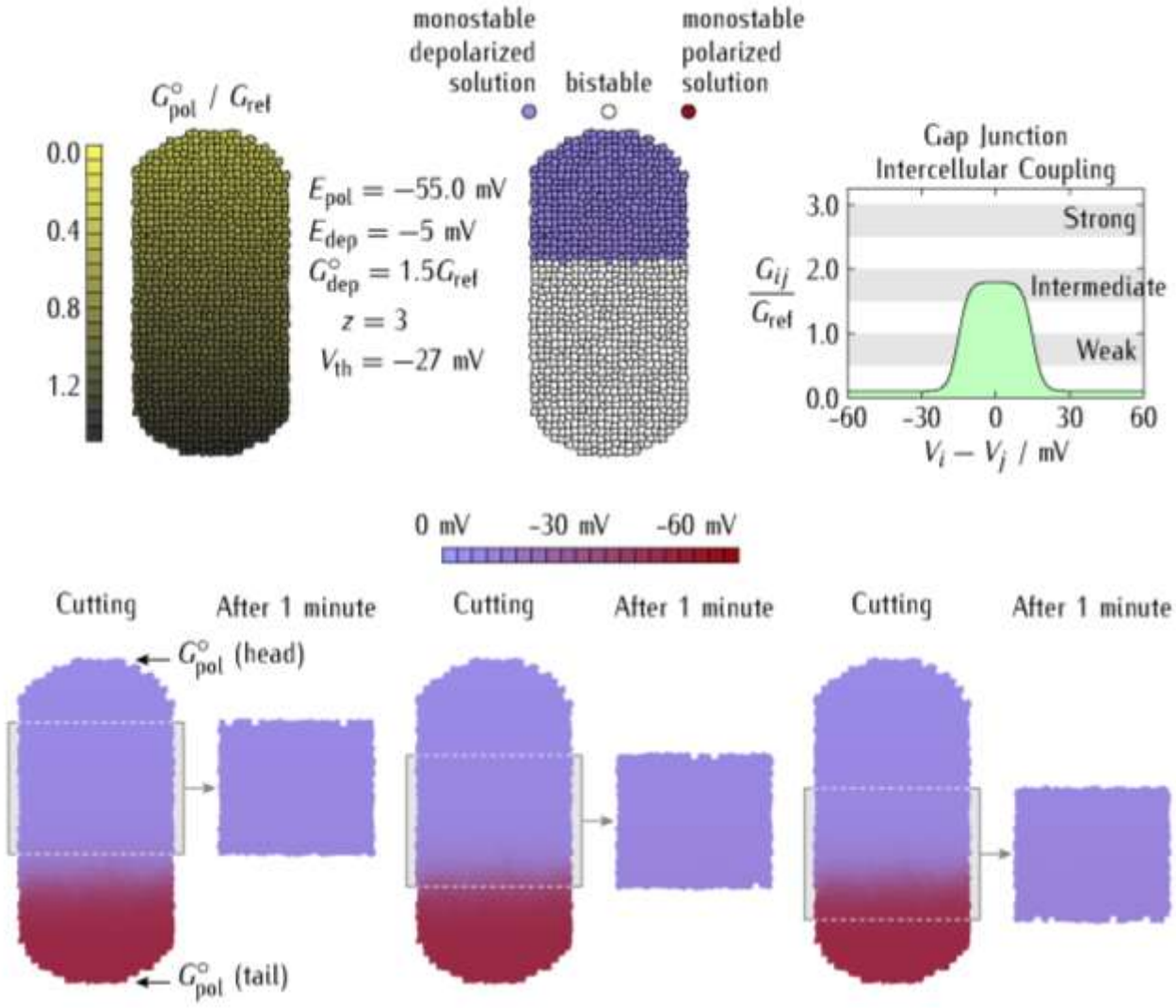

Schematic 5. The parameters and cell bioelectrical states characteristic of a multicellular ensemble (*top*). The only difference among the cells is the value of G°_{pol}, which varies linearly between $G^{\circ}_{\mathrm{pol}}/G_{\mathrm{ref}} = 1.4$ (bottom T cells) and $G^{\circ}_{\mathrm{pol}}/G_{\mathrm{ref}} = 0.4$ (top H cells). Note that the H cells are in a monostable depolarized state while the T cells are in a bistable region. After reaching the steady-state, the ensemble is sliced at three different positions of approximately the same size, which are then left to evolve until they reach the new state. Intermediate values for the maximum gap junction conductance are assumed (*top*, right).

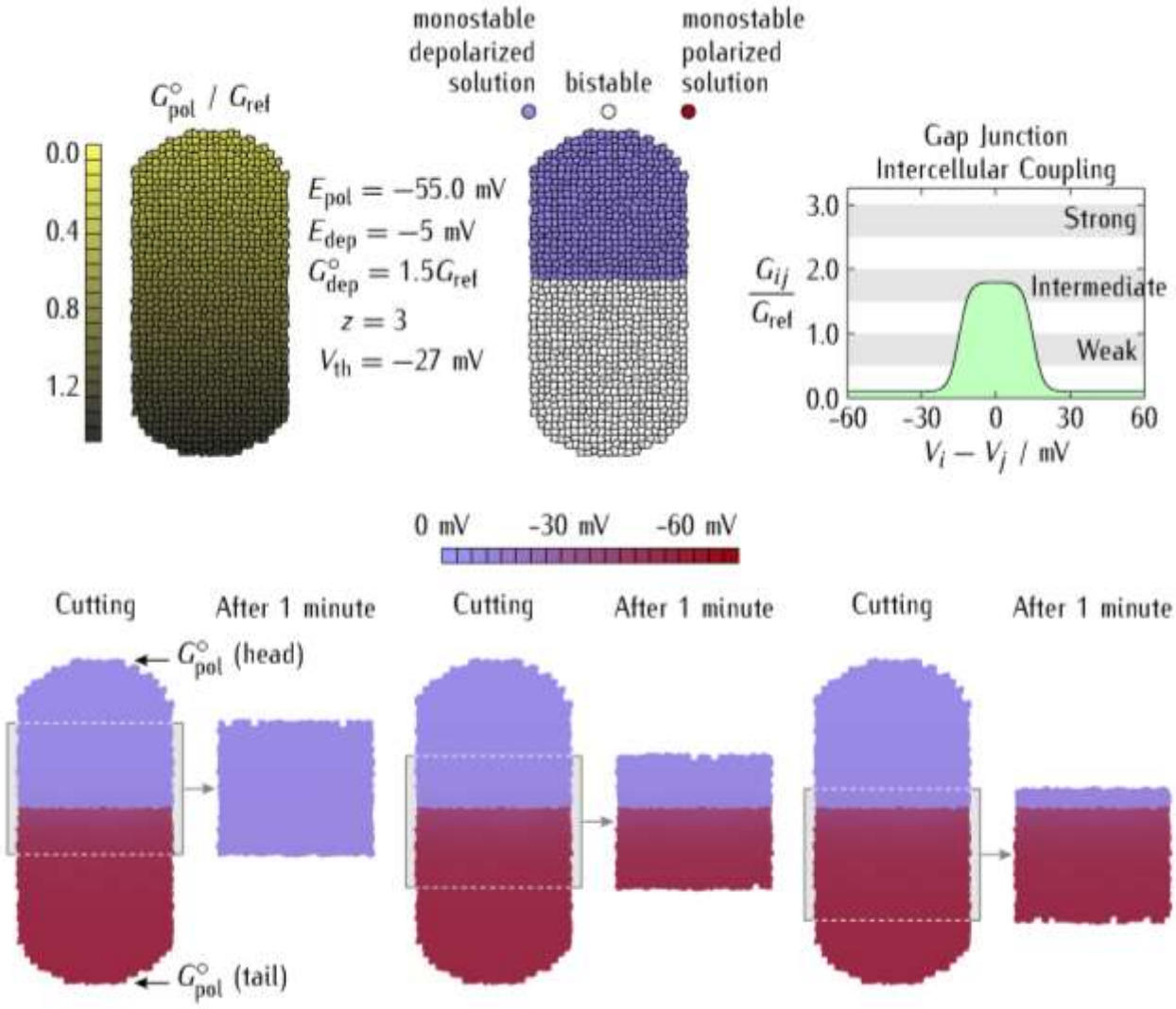

Schematic 6. The same system as in Schematic 5 except that now the vertical G°_{pol} gradient is made steeper by setting the H cells at the top to $G^{\circ}_{\mathrm{pol}}/G_{\mathrm{ref}} = 0.3$ instead of 0.4 (Schematic 5). In this case, both the cell potentials map and the three slices show abrupt transition regions between the depolarized and polarized regions. This result arises because of the closure of the gap junctions, which occurs when the potential difference among neighboring cells at the depolarized/polarized frontier increases.

The multicellular community effect allows the bulk of polarized T cells to resist depolarization in the slices of Schematic 6. This result can be checked by weakening the intercellular gap junctions, which occurs when they are blocked e.g. by adding octanol [16] to the slices. In the simulations, this external action can be modeled by decreasing the maximum junction conductance $G_{\mathrm{GJ,max}}$ after cutting

(Schematic 7). The decrease in the community effect that stabilized the bistable T cells in the polarized state before junction blocking (Schematic 6) allows the monostable H cells to enforce now the depolarized state through most of the slice (compare Schematic 7 with Schematic 6). Therefore, partial gap junction blocking (Schematic 7, *top, right*) does not necessarily lead to keeping the electrical regionalization in this case (Schematic 7, *bottom*) because decreasing the intercellular connectivity also weakens the community effect that allowed the initially polarized T cells to resist the effect of the dominant depolarized H cells. This counter-intuitive fact suggests that external actions aimed at decreasing the intercellular coupling could produce rather puzzling outcomes that depend on the particular bioelectrical states of the regions whose bioelectrical disconnection is attempted.

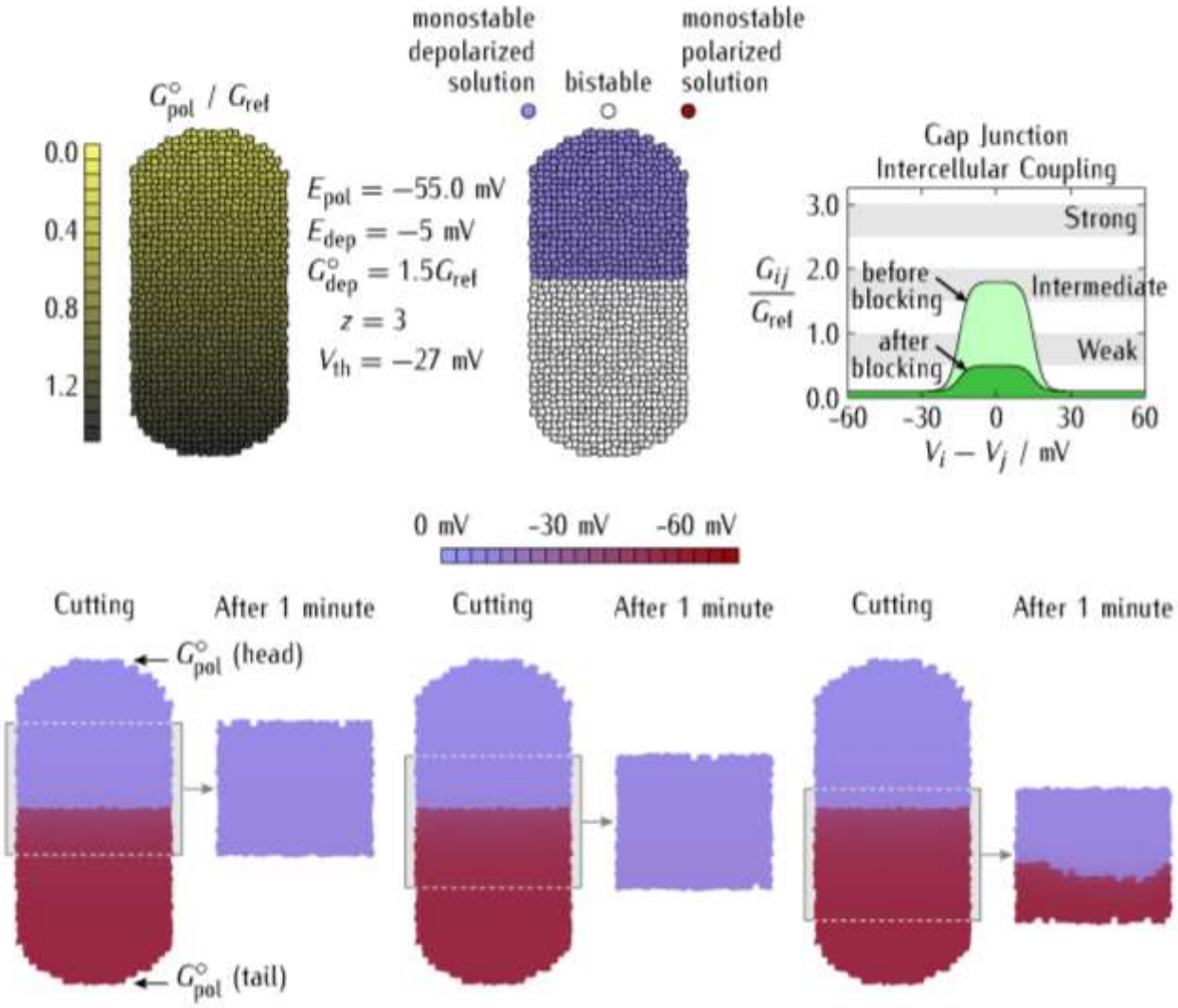

Schematic 7. We revisit the case of Schematic 6 but now, after the ensemble is sliced, the maximum value of the gap junction conductance is decreased to simulate the addition of a blocking agent. This external action weakens the community effect among the bistable polarized T cells and thus the monostable depolarized H cells can enforce depolarization through most of the slice. Compare these results with those of Schematic 6. In line with experimental data [16], low values for the maximum gap junction conductance are assumed after octanol addition (*top*, *right*).

Importantly, the consequences of reducing $G_{\mathrm{GJ,max}}$ are *context-dependent*: the effects observed in Schematics 6 (before blocking) and 7 (after blocking) are significantly different from those observed in Schematics 5 (before blocking) and 8 (after blocking). In the second case, Schematic 8 shows a partial tail repolarization with respect to Schematic 5 because the depolarized monostable regions of Schematics 5 and 8 are smaller than those of Schematics 6 and 7. These different system outcomes emphasize a collective property of the model: the interplay between the bi-stability of the polarized/depolarized single-cell state and the intercellular connectivity act together to give the multicellular bioelectrical state where all the cells in a fragment agree on which bioelectric state they will eventually reach. In this way, the individual cell states all agree on a final large-scale coherent outcome.

However, the above coherent outcome is not free from stochastic effects. The limited knowledge of the system bioelectric state, together with the experimental uncertainties associated with the exact determinations of the cutting plane position and the spatio-temporal map of multicellular connectivity, point out the difficulty of predicting the system transitions under *apparently identical* macroscopic conditions. Indeed, all these uncertainties should act together as sources of physiological noise whose eventual amplification will impact on the final morphological outcome leading to puzzling experimental results. Clearly, this fact also suggests that *additional control mechanisms* not considered here should be operative in real biological systems to enforce reliable outcomes [4,14,17] – an area in which the present model must be extended.

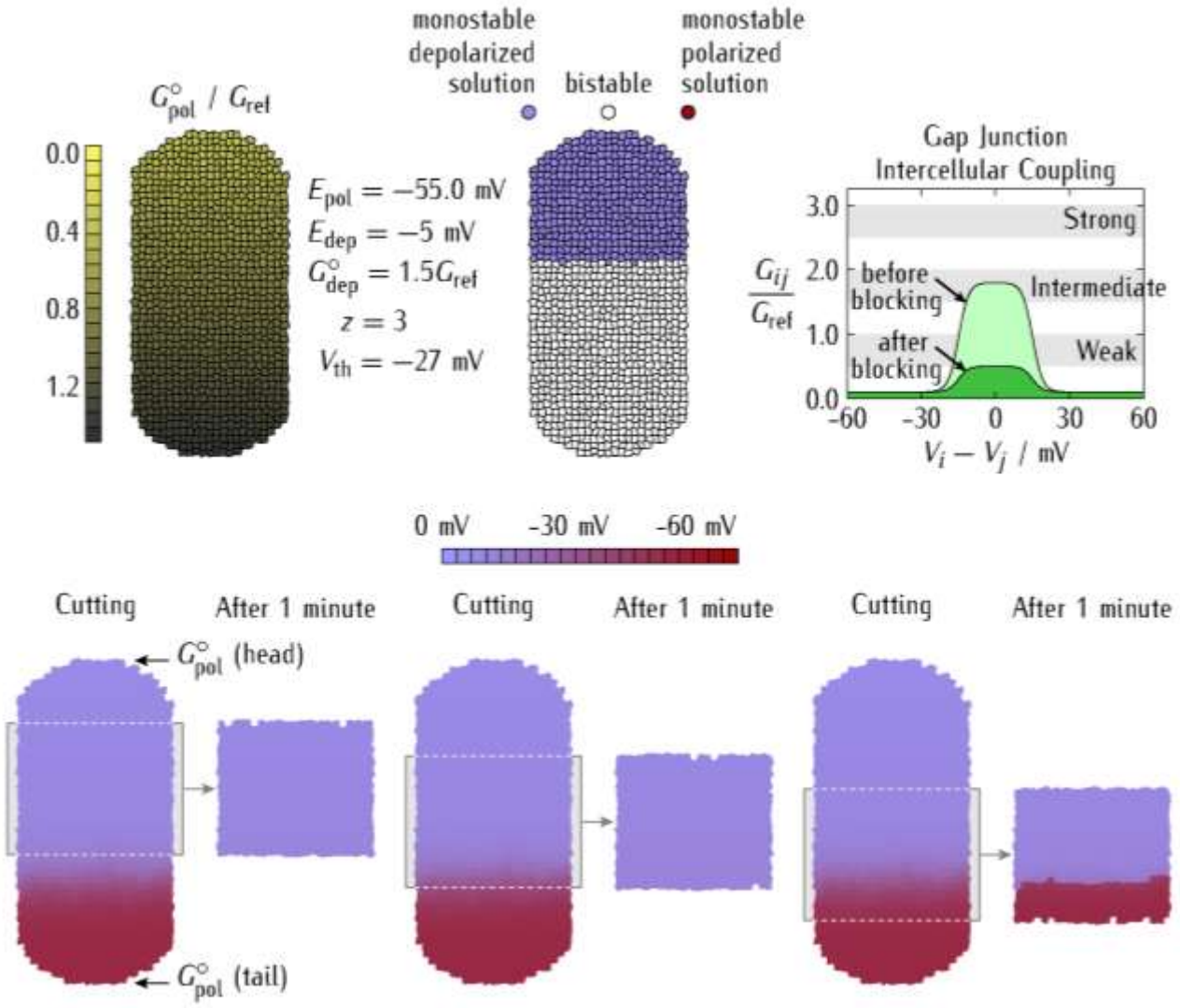

Schematic 8. The effect of gap junction blocking is context-dependent. If we consider initially the case of Schematic 5 instead of that of Schematic 6 and then proceed to decrease of the maximum junction conductance by blocking, a different outcome than that of Schematic 7 is obtained.

To better visualize the behavior of the ensemble under different conditions, Schematics 9–11 show the maps of steady-state cell potentials before and after cutting (central slice) for the conditions of Schematics 5 and 6. To reduce the number of varying parameters, only the maximum gap junction conductance $G_{\mathrm{GJ,max}}$ and the difference between the maximum *pol* channel conductance G°_{pol} between the T and H cells are changed, while the rest of parameters take the same values as in Schematics 5 and 6. The bottom T cells have always the *pol* channel conductance $G^{\circ}_{\mathrm{pol}}/G_{\mathrm{ref}} = 1.4$ while the rest of the

cells have conductances that vary linearly between the bottom T cells and the up H cells, as shown in the schematics.

Note the extension of the H depolarized region to the T polarized region in Schematics 9–11 as the *pol* channel conductance $G_{\mathrm{pol}}^{\mathrm{head}}/G_{\mathrm{ref}}$ decreases and then the difference $(G_{\mathrm{pol}}^{\mathrm{tail}}-G_{\mathrm{pol}}^{\mathrm{head}})/G_{\mathrm{ref}}$ increases. This extension is, however, less apparent for *high* than for *low* gap junction conductances (compare Schematic 11 with Schematic 9), in agreement with the effects observed in Schematic 6 (*high* intercellular conductances) and 8 (*low* intercellular conductances).

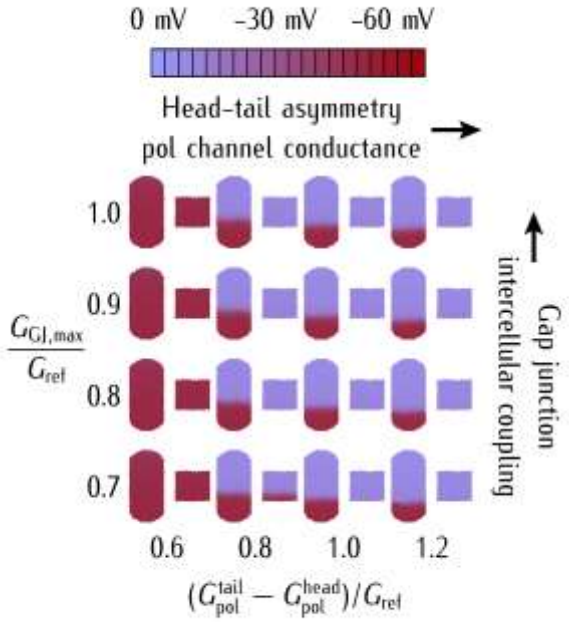

Schematic 9. The map of cell potentials before and after the central cut. To reduce the number of varying parameters, only the maximum gap junction conductance $G_{\mathrm{GJ,max}}/G_{\mathrm{ref}}$ and the difference between the maximum *pol* channel conductances at the tail ($G_{\mathrm{pol}}^{\mathrm{tail}}/G_{\mathrm{ref}}$) and the head ($G_{\mathrm{pol}}^{\mathrm{head}}/G_{\mathrm{ref}}$) are changed. The rest of system parameters are the same as in Schematics 5 and 6. In all cases, the conductance $G_{\mathrm{pol}}^{\mathrm{tail}}/G_{\mathrm{ref}}$=1.4 is decreased linearly from the bottom T cells to the top H cells to give the differences shown in the schematic. These simulations correspond to *low* intercellular conductances.

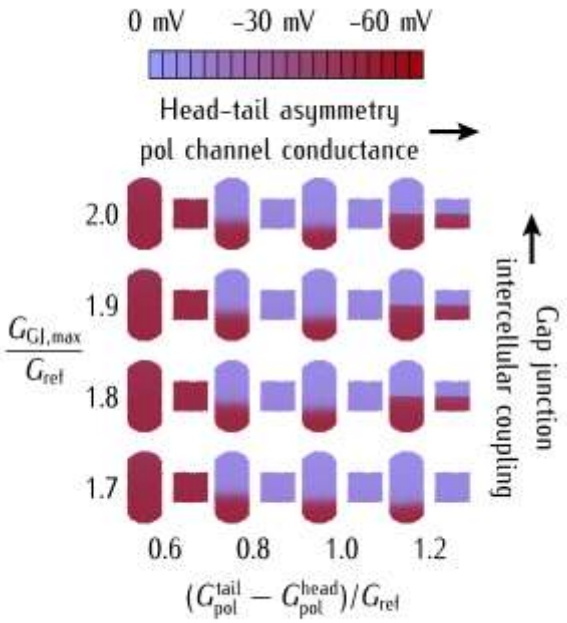

Schematic 10. The map of cell potentials before and after cutting for the conditions of Schematic 9, except for the maximum gap junction conductances that take now *intermediate* rather than low values. For comparison, Schematic 5 is obtained with $\left(G_{\mathrm{pol}}^{\mathrm{tail}} - G_{\mathrm{pol}}^{\mathrm{head}}\right)/G_{\mathrm{ref}} = 1.0$ while Schematic 6 corresponds to $\left(G_{\mathrm{pol}}^{\mathrm{tail}} - G_{\mathrm{pol}}^{\mathrm{head}}\right)/G_{\mathrm{ref}} = 1.1$, with $G_{\mathrm{GJ,max}}/G_{\mathrm{ref}} = 1.8$ for the two schematics. Note that in the second case the *pol* channel conductance and electric potential gradients are steeper than in the first case. This result leads to a closure of the voltage-gated intercellular conductance (Schematics 5 and 6, *right*, *top*) that enhances the electrical regionalization, which occurs when the *pol* channel conductance and electric potential gradients are made steeper. This result is apparent at the transition from $\left(G_{\mathrm{pol}}^{\mathrm{tail}} - G_{\mathrm{pol}}^{\mathrm{head}}\right)/G_{\mathrm{ref}} = 1.0$ to $\left(G_{\mathrm{pol}}^{\mathrm{tail}} - G_{\mathrm{pol}}^{\mathrm{head}}\right)/G_{\mathrm{ref}} = 1.2$ at $G_{\mathrm{GJ,max}}/G_{\mathrm{ref}} = 1.8 - 2.0$.

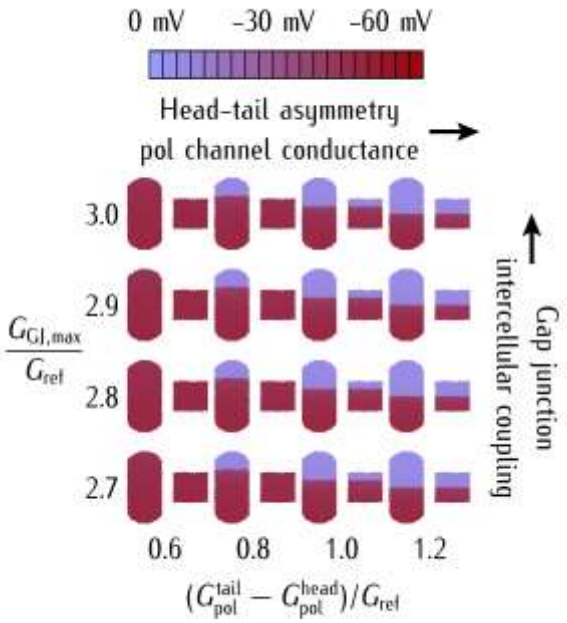

Schematic 11. The map of cell potentials before and after cutting for the conditions of Schematic 10, except for the maximum gap junction conductances that take now *high* rather than intermediate values. Note the effect due to the closure of the voltage-gated intercellular conductance and the resulting electrical regionalization, which occurs when the *pol* channel conductance and electric potential gradients are made steeper.

The distinct outcomes obtained by slightly changing the *pol* channel conductance difference $(G_{\mathrm{pol}}^{\mathrm{tail}}-G_{\mathrm{pol}}^{\mathrm{head}})/G_{\mathrm{ref}}$ and the gap junction conductance $G_{\mathrm{GJ,max}}/G_{\mathrm{ref}}$ in Schematics 9–11, together with the marked dependence of these outcomes on the cutting planes in Schematics 5–8, strongly suggest that significant variability effects should be observed when attempting to manipulate planarian development and regeneration under *supposedly identical* conditions [4,14]. Despite the experimental uncertainties inherent to interacting ensembles composed of cells with non-linear individual behaviors, Schematics 9–11 together with the phase space of Schematic 3 show that bioelectric spatio-temporal maps can have significant connections with regenerative outcomes because they allow *establishing and maintaining positional indications* towards development. In real systems, however, these constraints

should act in concert with additional biochemical signals ignored here; see Figs. 5 of Ref. [14] and 3 of Ref. [4] in this context.

The biophysical model described here can also be extended to include a spatially-inhomogeneous distribution of intercellular gap junctions (see e.g. Fig. 8 of Ref [21]), which should be useful for the theoretical description of experiments concerning the spatially-regionalized blocking of specific ion channels and gap junctions [16,22].

4. Discussion and conclusions

A new theoretical model that emphasizes bioelectrical *single-cell* characteristics such as membrane ion channels and pumps and includes *multicellular community* effects via voltage-gated gap junctions has been described. Although this simple biophysical approach ignores important biochemical processes, it can provide qualitative insights concerning intercellular coupling, cutting plane, and gap junction blocking of the multicellular ensemble. In particular, we have attempted to relate our simulations to recent experiments concerning planarian anterior/posterior bioelectrical polarity [4,14,17]. Some of the theoretical predictions of the two-cell and multicellular models are in qualitative agreement with the experimental observations (1–4) while others (5 and 6) are at variance with them:

1) Regeneration models should address a crucial problem: which mechanism allows separated cell domains to determine their relative position and how this mechanism can be restored after injury [3,14,18,24]. In qualitative agreement with recent experiments [4,14], both models used here show how bioelectrical signals can play such a role in the final system outcomes.

2) In the two-cell model, the use of polarizing agents such as H,K-ATPase inhibitors (SCH) that increase the potential difference $V_{\mathrm{H}}^{\circ} - V_{\mathrm{T}}^{\circ}$ at constant gap junction conductance $G_{\mathrm{GJ,max}}/G_{\mathrm{ref}}$ can facilitate the transition from the abnormal DH state to the normal H–T state; on the contrary,

depolarizing agents such as the nigericin ion pump will favor the inverse process. For high enough values of the conductance $G_{\mathrm{GJ,max}}/G_{\mathrm{ref}}$, these transitions between the DH and H–T states will occur through a bi-stability region that the model interprets as the cryptic state region. In principle, these general conditions should also be applicable to the multicellular case, as suggested by the results of Schematics 9–11.

3) Externally-induced closing of the gap junction by a blocking agent such as octanol leads to low intercellular conductances $G_{\mathrm{GJ,max}}/G_{\mathrm{ref}}$ whose effects are *context-dependent* (Schematic 3). At constant *low* potential differences $V_{\mathrm{H}}^{\circ} - V_{\mathrm{T}}^{\circ}$, the decrease of $G_{\mathrm{GJ,max}}/G_{\mathrm{ref}}$ will not change the DH state. At constant *high* values of $V_{\mathrm{H}}^{\circ} - V_{\mathrm{T}}^{\circ}$, however, the decrease of $G_{\mathrm{GJ,max}}/G_{\mathrm{ref}}$ may trigger the system transition from the cryptic to the normal H–T state. In the case of the multicellular ensemble, however, Schematics 5–8 show a more complex behavior including system regionalization.

4) In the two-cell model also, when both the potential difference $V_{\mathrm{H}}^{\circ} - V_{\mathrm{T}}^{\circ}$ and the gap junction conductance $G_{\mathrm{GJ,max}}/G_{\mathrm{ref}}$ are simultaneously decreased, the addition of a junction-blocking agent may favor the transition between the normal H–T state and the cryptic and abnormal DH states. In the particular case of the two-cell model (Schematic 3), this transition should be easier at *lower* (*bottom* of the bi-stability region) than at *higher* (*top* of the bi-stability region) values of the potential difference $V_{\mathrm{H}}^{\circ} - V_{\mathrm{T}}^{\circ}$.

5) While the model does not give any fixed value for the frequency of DH worms arising from cutting cryptic worms [14] that could be compared to the experimentally-observed constant ratio, it identifies the bioelectrical parameters that regulate the transitions. In the two-cell

model, it is the relative bioelectrical distance of the cryptic state to the monostable DH and H-T states in the phase space of the system that should give the probability to eventually reach one of these sates after cutting. Experimentally, the ion channels and pumps that establish the potential difference $V_{\mathrm{H}}^{\circ} - V_{\mathrm{T}}^{\circ}$ and the gap junction proteins that modulate the intercellular connectivity $G_{\mathrm{GJ,max}}/G_{\mathrm{ref}}$ can shift the above transition probability by changing the relative distance of the cryptic state to the monostable DH (*left*) and H-T (*right*) states of Schematic 3.

6) In the multicellular model, context-dependent responses can be obtained as a function of the exact cutting plane position, the initial system bioelectrical state, and the multicellular connectivity. These experimental uncertainties must lead to significant physiological noise effects that will eventually impact on the final morphological outcome unless other control mechanisms not included in the model make appropriate corrections during development. The above facts point out the difficulty of predicting the system transitions under *apparently identical* macroscopic conditions. Remarkably, some general conclusions should still apply. For instance, those position cuts significantly decreasing the potential difference $V_{\mathrm{H}}^{\circ} - V_{\mathrm{T}}^{\circ}$ at constant gap junction conductance $G_{\mathrm{GJ,max}}/G_{\mathrm{ref}}$ will more likely give DH rather than cryptic states. As to other types of cuts, however, we note that half length-wise cuts of narrow fragments that are lateral "brothers" might have different system outcomes [4]. In the context of the present model, this would suggest that other spatial asymmetries different than the axially inhomogeneous distribution of ion channels assumed in Schematic 5 (*top*) are present. We note here that a complete description of body-plan axis in regenerating planaria emphasizing additional (neural) mechanisms of control has recently been given [17]. In this quantitative study, target morphology is encoded by vector transport fields associated with the neural architecture [17].

It is remarkable that the models of Schematics 2 and 4 constitute *two-cell and multicellular distributed memories*, respectively. The bioelectrical states characteristic of these *memories are encoded in the spatio-temporal distribution* of electric potential that will eventually influence the local concentration of signaling ions and molecules [22]; see the left insets of Schematics 2 and 4. These distributions are regulated by the single-cell and intercellular channel conductances that support $V_{\mathrm{H}}^{\circ} - V_{\mathrm{T}}^{\circ}$ and G_{GJ} (Schematics 3 and 5–8). Note also that in addition to bioelectrical gating, these magnitudes can also be gated biochemically in the model, e.g. by blocking the above channels with external agents (Schematic 7) [18,22,25] or by changing the ionic concentrations that establish the equilibrium potentials E_{dep} and E_{pol} (Schematic 2) [24,25].

In summary, ion channels and endogenous bioelectric fields [13,22,26-28] can introduce new ideas concerning the anterior-posterior identity of regenerating wounds and the electrical response to injury [4,14,18,29], provide insight into the system-level dynamics of stochastic patterning systems [14,17], and are a complement to molecular morphogenetic studies [30,31] and single-cell events regulating stem cell differentiation in planaria [32,33]. Future research will expand on this work by building more detailed models of specific patterning systems that encompass bioelectric controls and downstream gene expression cascades together with the physical forces that implement morphogenesis. Moreover, such insights will be essential for the nascent field of synthetic morphology [34-37], which seeks to harness emergence and guided self-assembly of cellular processes towards the rational control of structure and function in novel biological forms.

References

[1] T. Stückemann, J. P. Cleland, S. Werner, H. T.-K. Vu, R. Bayersdorf, S. Liu, B. Friedrich, F. Jülicher, J. C. Rink, Antagonistic self-organizing patterning systems control maintenance and regeneration of the anteroposterior axis in planarians. Dev. Cell. 40 (2017) 248–263.

[2] P. W. Reddien, The Cellular and Molecular Basis for Planarian Regeneration. Cell 175 (2018) 327–345.

[3] A. G. Tewari, S. R. Stern, I. M. Oderberg, P. W. Reddien, Cellular and Molecular Responses Unique to Major Injury Are Dispensable for Planarian Regeneration . Cell Reports 25 (2018) 2577–2590.

[4] F. Durant, J. Bischof, C. Fields, J. LaPalme, A. Hoi, M. Levin, The role of early bioelectric signals in the regeneration of planarian anterior/posterior polarity. Biophys. J. 116 (2019) 948–961.

[5] C. S. Lange, V. E. Steele, The mechanism of anterior-posterior polarity control in planarians. Differentiation. 11 (1978) 1–12.

[6] K. L. Abdul, M. Stacey, R. Barrett-Jolley, Emerging Roles of the Membrane Potential: Action Beyond the Action Potential. Front Physiol. 9 (2018) 1661.

[7] I. Weiß, J. Bohrmann. Electrochemical patterns during Drosophila oogenesis: ion-transport mechanisms generate stage-specific gradients of pH and membrane potential in the follicle-cell epithelium. BMC Developmental Biology 19 (2019) 12.

[8] Y. Wang, X. Han, Z. Cui, and D. Shi, Bioelectricity, Its Fundamentals, Characterization Methodology, and Applications in Nano-Bioprobing and Cancer Diagnosis. Adv. Biosys. (2019) 1900101.

[9] N. Luo, S. Wang, L. You, Synthetic Pattern Formation. Biochemistry 58 (2019) 1478−1483.

[10] H. Meinhardt, Turing's theory of morphogenesis of 1952 and the subsequent discovery of the crucial role of local self-enhancement and long-range inhibition. Interface Focus 2 (2012) 407–416.

[11] E. P. Olimpio, Y. Dang, H. Youk, Statistical Dynamics of Spatial-Order Formation by Communicating Cells. iScience 2 (2018) 27–40,.

[12] H. M. McNamara, H. Zhang, C. A. Werley, A. E. Cohen, Optically controlled oscillators in an engineered bioelectric tissue. Phys. Rev. X 6 (2016) 031001.

[13] J. Cervera, A. Pietak, M. Levin, S. Mafe, Bioelectrical coupling in multicellular domains regulated by gap junctions: a conceptual approach. Bioelectrochem. 123 (2018) 45–61.

[14] F. Durant, J. Morokuma, C. Fields, K. Williams, D.S. Adams, M. Levin, Long-Term, Stochastic Editing of Regenerative Anatomy via Targeting Endogenous Bioelectric Gradients, Biophys, J. 112 (2017) 2231−2243.

[15] K. A. McLaughlin, M. Levin, Bioelectric signaling in regeneration: Mechanisms of ionic controls of growth and form, Dev. Biol. 433 (2018) 177–189.

[16] M. Emmons-Bell, F. Durant, J. Hammelman, N. Bessonov, V. Volpert, J. Morokuma K. Pinet, D.S. Adams, A. Pietak, D. Lobo, M. Levin, Gap junctional blockade stochastically induces different species-specific head anatomies in genetically wild-type Girardia dorotocephala flatworms, Int. J. Mol. Sci. 16 (2015) 27865–27896.

[17] A. Pietak, J. Bischof, J. LaPalme, J. Morokuma, M. Levin, Neural control of body-plan axis in regenerating planaria. PLoS Comput. Biol. 15 (2019) e1006904.

[18] T. H. Peiris, N. J. Oviedo, Gap junction proteins: Master regulators of the planarian stem cell response to tissue maintenance and injury. Biochimica et Biophysica Acta 1828 (2013) 109–117.

[19] D. Lobo, M. Levin, Computing a worm: reverse-engineering planarian regeneration. *Advances in Unconventional Computing*. Andrew Adamatzky ed. (2016) Vol. 2, Springer, 637–654.

[20] A. G. Volkov, S. Toole, M. Maina, Electrical signal transmission in the plant-wide web. Bioelectrochem.129 (2019) 70–78.

[21] J. Cervera, S. Meseguer, S. Mafe, The interplay between genetic and bioelectrical signaling permits a spatial regionalisation of membrane potentials in model multicellular ensembles. Sci. Rep. 6 (2016) 35201.

[22] J. Cervera, V. P. Pai, M. Levin, S. Mafe, From non-excitable single-cell to multicellular bioelectrical states supported by ion channels and gap junction proteins: electrical potentials as distributed controllers. Progress Biophys. Mol. Biol. (2019) DOI: 10.1016/j.pbiomolbio.2019.06.004.

[23] S. Baigent, J. Stark, A. Warner, Modelling the effect of gap junction nonlinearities in systems of coupled cells, J. Theor. Biol. 186 (1997) 223–239.

[24] B. Reid, M. Zhao, The Electrical Response to Injury: Molecular Mechanisms and Wound Healing. Adv. Wound Care (New Rochelle) 3 (2014) 184–201.

[25] B. Hille, Ion channels of excitable membranes, 3rd ed., Sinauer Associates, 1992.

[26] E. Bates, Ion channels in development and cancer. Annu. Rev. Cell Dev. Biol. 31 (2015) 231–247.

[27] R. H. W. Funk, Ion Gradients in Tissue and Organ Biology. Biol. Syst. Open Access 2 (2013) 1000105.

[28] H. M. McNamara, H. Zhang, C. A. Werley, A. E. Cohen, Optically Controlled Oscillators in an Engineered Bioelectric Tissue. Phys. Rev. X 6 (2016) 031001.

[29] A. Pietak, M. Levin, Bioelectrical control of positional information in development and regeneration: A review of conceptual and computational advances. Prog. Biophys. Mol. Biol. 137 (2018) 52–68.
[30] T. Stückemann, J. P. Cleland, S. Werner, H. T.-K. Vu, R. Bayersdorf, S.-Y. Liu, B. Friedrich, F. Jülicher, J. C. Rink, Antagonistic Self-Organizing Patterning Systems Control Maintenance and Regeneration of the Anteroposterior Axis in Planarians. Dev. Cell. 40 (2017) 248–263.
[31] T. Adell, F. Cebrià, E. Saló, Gradients in planarian regeneration and homeostasis. Cold Spring Harb. Perspect. Biol. 2 (2010) a000505.
[32] S. Owlarn, K. Bartscherer, Go ahead, grow a head! A planarian's guide to anterior regeneration. Regeneration 3 (2016) 139–155.
[33] A. Rozanski, H. Moon, H. Brandl, J. M. Martín-Durán, M. A. Grohme, K. Hüttner, K. Bartscherer, I. Henry, J. C. Rink, PlanMine 3.0-improvements to a mineable resource of flatworm biology and biodiversity. Nucleic Acids Res. 47 (2019) D812–D820.
[34] R. D. Kamm, R. Bashir, Creating living cellular machines. Ann. Biomed. Eng. 42 (2014) 445–459.
[35] A. Ollé-Vila, S. Duran-Nebreda, N. Conde-Pueyo, R. Montañez, R. Solé, A morphospace for synthetic organs and organoids: the possible and the actual. Integr. Biol. (Camb). 8 (2016) 485–503.
[36] F. Varenne, P. Chaigneau, J. Petitot, R. Doursa, Programming the Emergence in Morphogenetically Architected Complex Systems. Acta Biotheoretica 63 (2015) 295–308.
[37] J. J. Velazquez, E. Su, P. Cahan, M. R. Ebrahimkhani, Programming Morphogenesis through Systems and Synthetic Biology. Trends Biotechnol. 36 (2018) 415–429.